INL/EXT-15-34786

Light Water Reactor Sustainability Program

Crystal Plasticity Model of Reactor Pressure Vessel Embrittlement in Grizzly

July 2015

DOE Office of Nuclear Energy

INL/EXT-15-34786

Light Water Reactor Sustainability Program

Crystal Plasticity Model of Reactor Pressure Vessel Embrittlement in Grizzly

Pritam Chakraborty,
S. Bulent Biner,
Yongfeng Zhang,
Benjamin Spencer

[1]Idaho National Laboratory

July 2015

Idaho National Laboratory
Idaho Falls, Idaho 83415

http://www.inl.gov/lwrs

Prepared for the
U.S. Department of Energy
Office of Nuclear Energy
Under DOE Idaho Operations Office
Contract DE-AC07-05ID14517

EXECUTIVE SUMMARY

The integrity of reactor pressure vessels (RPVs) is crucial to ensure safe operation of nuclear reactors under extended lifetime. Microstructure scale models at various length and time scales, coupled concurrently or through homogenization methods, can play a significant role in understanding and quantifying irradiation induced defect production, growth and their influence on mechanical behavior of RPV steels. A multi-scale approach, involving atomistic, meso and engineering scale models, is currently being pursued within the Grizzly project to understand and quantify irradiation induced embrittlement of RPV steels. Within this framework, a dislocation-density based crystal plasticity model has been developed in Grizzly that captures the effect of irradiation induced defects on the flow stress behavior and is presented in this report. The present formulation accounts for the interaction between self-interstitial loops and matrix dislocations. The model predictions have been validated with experiments and compared against dislocation dynamics simulations.

CONTENTS

FIGURES

1 Introduction

The long-term exposure of reactor pressure vessels (RPVs) to irradiation causes precipitation and segregation of secondary phases and formation and growth of defect clusters and loops. These irradiation induced defects embrittle the RPV steels and increase their propensity to catastrophic failure [1]. For instance, with increasing fluence an increase in the yield stress is typically observed. Also, the ductile-to-brittle transition temperature (DBTT) has been observed to increase with irradiation dose levels. Hence, to ensure safe extension of operational lifetime of nuclear reactors, accurate assessment of RPV steel embrittlement is essential.

The present approaches to quantify embrittlement in RPVs rely on semi-empirical models that are calibrated using the surveillance samples in the reactors [2]. Though these models have successfully quantified DBTT shifts and yield stress increase for the purpose of life extension from 40-60 years, their accuracy for future predictions can be hindered due to the lack of experimental data. Multi-scale models of irradiation induced aging can assist in improving the predictive ability of the semi-empirical models by providing surrogate data, as well as identifying mechanisms that can emerge due to longer exposures beyond the designed period [3]. These models span widely differing length and time-scales from atomistics to engineering scale, and provide physical understanding of defect formation, their interaction and effect on mechanical behavior.

At the scale of fracture specimens, the models developed to characterize DBTT shifts primarily incorporate the mechanisms causing stable ductile damage and probabilistic cleavage initiation. For ductile damage, pressure sensitive plasticity models characterizing void nucleation, growth and coalescence are utilized [4, 5]. The model parameters are calibrated from tensile tests and/or fracture tests at the upper shelf. The cleavage initiation models are based on the weakest link theory, which incorporates the mechanism of plasticity induced micro-crack formation from grain-boundary carbides and their growth into a macro-crack causing unstable failure. The Beremin model [6], which uses the weakest link theory-based Weibull distribution [7] for probabilistic cleavage initiation, is employed to capture the scattered fracture energy and toughness data observed in the transition regime. The Beremin model parameters are calibrated near the lower shelf.

A combination of the ductile damage and Beremin model has been used in finite element (FE) simulations of fracture specimens to obtain DBTT by several authors [8, 9, 10]. In [10], the calibrated damage parameters are kept constant and only the temperature-sensitive flow stress is varied to obtain the DBTT of unirradiated RPV steels. In [8], temperature dependent Beremin model parameters are considered additionally to obtain improved comparison with experiments. Under irradiated conditions, it has been observed that both the ductile damage and cleavage model parameters vary with fluence [9]. In a parametric study using tensile test data for ferritic-martensitic steels [11], it has been shown that the effect of varying the ductile damage parameters saturates with increasing fluence, whereas flow stress parameters still evolve. From these numerical studies it can be concluded that accurate characterization of flow stress variation with temperature and irradiation dose levels is essential to evaluate DBTT shifts. Also, quantifying the yield stress variations alone is not sufficient to obtain the DBTT shifts and evaluation of flow stress variations until some cut-off plastic strain is necessary [12].

Modeling the evolution of flow stress with irradiation involves the development of methods to track defect evolution and its interaction with dislocations. Atomistic scale method such as Molecular Dynamics (MD) can provide insight into the fundamental mechanisms and the associated energetics. Coarse grained methods such as adaptive Kinetic Monte Carlo (aKMC) and Dislocation Dynamics (DD), can subsequently utilize the information from MD to model larger representative volumes for longer time. Meso-scale methods such as phase-field, cluster dynamics and crystal plasticity can further extend the length and time scales of defect evolution and interaction to poly-crystalline systems. The predictions from the crystal-plasticity models can then be utilized to define the flow stress variations at the specimen-scale simulations. Hence in the present work, a crystal plasticity based modeling approach is being developed to quantify the interaction between irradiation induced defects and dislocations with the objective of obtaining correlations between irradiation fluence and flow stress variations in RPV steels.

The nucleation and growth of irradiation induced Cu, Ni and Mn precipitates is one of the sources of embrittlement in RPV steels [1]. These precipitates act as obstacles to dislocation motion and increase the yield stress of the irradiated material. Point defect clusters and loops have also been observed to significantly influence the flow stress behavior of ferritic and ferritic/martensitic steels [13]. The irradiation induced prismatic self-interstitial atomic (SIA) loops have been observed to obstruct dislocation motion, which increases the yield stress of the material. However, as the dislocations are unpinned they annihilate the SIA loops causing the formation of defect free channels. The formation of such clear channels have been observed experimentally and can explain the loss of strain-hardening capacity in ferritic/martensitic steels irradiated to high dose-levels [13].

The crystal plasticity models presented in this report investigate the variation of flow stress with irradiation by considering the interaction between prismatic SIA loops and network dislocations. In the first model, the prismatic loops are assumed to be present on all the slip-systems and the annihilation of the defect loops is incorporated by a decreasing loop density rate with mobile dislocations [14]. RPV steels have a BCC crystallographic system and the cross-slip of screw dislocations via double-kink mechanism has been observed to influence the flow behavior significantly in these materials. The cross-slip mechanism has been addressed in the first model and incorporated using a critical stress driven activation energy based law. The second model presented in this report extends the first model by considering the SIA loops on specific crystallographic planes ($1/2\langle 111\rangle$ and $\langle 100\rangle$) and their annihilation by mobile dislocations using a damage tensor [15]. Both these models have subsequently been validated with experiments [16] and dislocation dynamics simulation [17], respectively.

2 Dislocation-density based crystal plasticity model

In the crystal plasticity model [18], the deformation gradient tensor, $\underline{\underline{F}}$, is multiplicatively split as

$$\underline{\underline{F}} = \underline{\underline{F}}^e \underline{\underline{F}}^p \tag{1}$$

where $\underline{\underline{F}}^e$ and $\underline{\underline{F}}^p$ are the elastic and plastic deformation gradients, respectively. The multiplicative split assumes an intermediate configuration where inelastic deformation occurs through dislocation motion along specific slip systems. This configuration is subsequently stretched and rotated elastically to the current configuration. A schematic of the initial, intermediate and current configurations at a time in the deformation history is shown in Fig. 1.

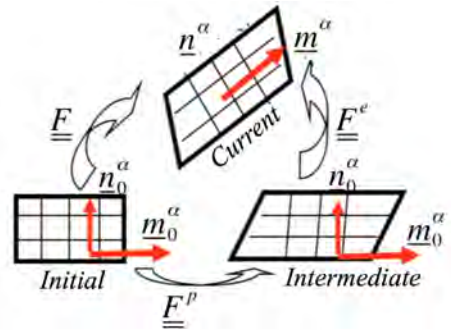

Figure 1: Multiplicative decomposition of the deformation gradient and the associated configurations at a time in the deformation history.

The rate of evolution of $\underline{\underline{F}}^p$ occurs through glide of dislocations along different slip systems as

$$\dot{\underline{\underline{F}}}^p = \sum_\alpha \dot{\gamma}^\alpha \underline{m}_0^\alpha \otimes \underline{n}_0^\alpha \tag{2}$$

where $\dot{\gamma}^\alpha$ is the glide rate on an individual slip system, α, and, $\underline{m}_0^\alpha$ is the direction of glide and $\underline{n}_0^\alpha$ is the slip plane normal in the intermediate configuration. The glide rate on a slip system in Eq. 2 evolves following Orowan's equation

$$\dot{\gamma}^\alpha = \rho_M^\alpha b^\alpha v^\alpha \tag{3}$$

where ρ_M^α is the density of mobile dislocation, b^α is the Burger's vector and v^α is velocity of mobile dislocations on the slip system. The v^α is defined using the activation enthalpy driven flow rule [14] as

$$v^\alpha = \begin{cases} l^\alpha \nu \exp\left(-\frac{\Delta F}{K_B T}\left(1 - \left[\frac{|\tau^\alpha| - s_a^\alpha}{s_t^\alpha}\right]^p\right)^q\right) sgn\left(\tau^\alpha\right), & \text{for } |\tau^\alpha| > s_a^\alpha \\ 0, & \text{otherwise} \end{cases} \tag{4}$$

where l^α is the average dislocation glide distance between barriers, ν is the jump frequency, ΔF is the activation energy under zero stress, K_B is Boltzmann's constant, T is the absolute temperature, τ^α is the resolved shear stress, and, s_a^α and s_t^α are the athermal and thermal resistances to slip, respectively. The resolved shear stress τ^α is related to the 2^{nd} Piola-Kirchhoff stress in the intermediate configuration ($\underline{\underline{T}}^*$) following

$$\tau^\alpha = \underline{\underline{T}}^* : \underline{m}_0^\alpha \otimes \underline{n}_0^\alpha \tag{5}$$

The evolution of s_a^α is based on the dispersed barrier hardening model [14]

$$s_a^\alpha = Gb^\alpha \sqrt{\sum_\beta q_p A^{\alpha\beta} \rho^\beta} \tag{6}$$

where G is the shear modulus, $A^{\alpha\beta}$ is the matrix with interaction coefficients of dislocations between different slip systems, q_p is a parameter and ρ^α is the total dislocation density on a slip system ($\rho^\alpha = \rho_M^\alpha + \rho_I^\alpha$) with contributions from mobile and immobile dislocations (ρ_I^α). The athermal slip resistance s_t^α depends on short-range obstacles and is related to the Peierl's barrier for BCC system [14]. The evolution of ρ_M^α follows [14]

$$\dot{\rho_M^\alpha} = \frac{k_{mul}}{b^\alpha} \sqrt{\sum_\beta \rho_M^\beta} \, |\dot{\gamma}^\alpha| + \dot{\rho}_{CS}^\alpha - \frac{2R_c}{b^\alpha} \rho_M^\alpha \, |\dot{\gamma}^\alpha| - \frac{1}{b^\alpha \lambda^\alpha} \, |\dot{\gamma}^\alpha| \tag{7}$$

where the first term represents dislocation multiplication following the Frank-Reed mechanism. The second term is the contribution from cross-slip of screw dislocations. The third term represents annihilation of dislocations of opposite signs, and, the fourth term represents the immobilization of dislocations due to trapping by pre-existing immobile dislocations and defects. In Eq. 7, k_{mul} is a multiplication factor, R_c is the annihilation radius of dislocations with opposite signs and λ^α is the mean trapping distance defined as $\frac{1}{\lambda^\alpha} = \beta_\rho \sqrt{\rho^\alpha}$. The evolution of ρ_I^α is defined as

$$\dot{\rho_I^\alpha} = \frac{1}{b^\alpha \lambda^\alpha} \, |\dot{\gamma}^\alpha| - k_{dyn} \rho_I^\alpha \, |\dot{\gamma}^\alpha| \tag{8}$$

where the second term represents the dynamic recovery of the immobile dislocations and k_{dyn} is a dynamic recovery factor.

There are a total of 48 slip systems in a BCC crystal system, including 12 $\langle 111 \rangle \{100\}$, 12 $\langle 111 \rangle \{112\}$ and 24 $\langle 111 \rangle \{123\}$. A schematic of these slip systems is shown in Fig.2. Conversely, each of the 4 $1/2 \langle 111 \rangle$ slip directions is associated with 12 slip planes.

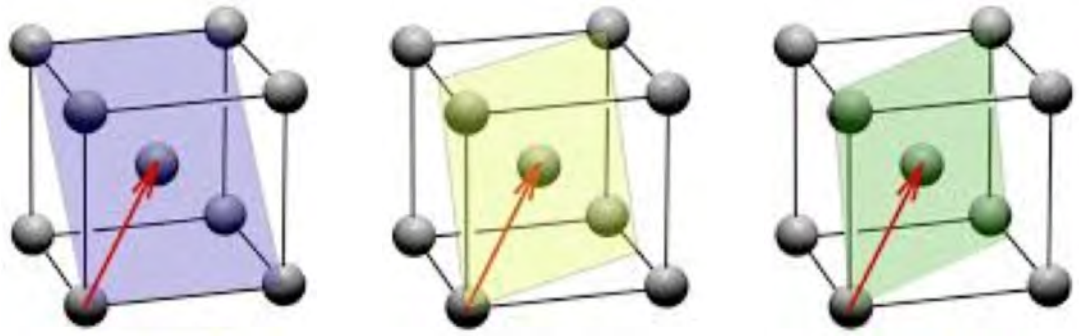

(a) (b) (c)

Figure 2: Family of slip systems in BCC crystal: (a) $\langle 111 \rangle \{100\}$; (b) $\langle 111 \rangle \{112\}$; (c) $\langle 111 \rangle \{123\}$.

Owing to such a crystallography in BCC system, screw dislocations along a slip direction can cross-slip on any of the 12 planes via a double-kink mechanism. The mechanism of cross-slip is thermally activated and is defined using a critical stress based law following

$$\dot{\rho}^{\alpha}_{CS} = \sum_{\beta\in\Phi,\beta\neq\alpha} k_{cs} exp\left(-\frac{(\tau^{*} - |\tau^{\alpha}|)\, V_a}{K_B T}\right) \rho^{\beta}_{M} \left|\dot{\gamma}^{\beta}\right| - \sum_{\beta\in\Phi,\beta\neq\alpha} k_{cs} exp\left(-\frac{\left(\tau^{*} - \left|\tau^{\beta}\right|\right) V_a}{K_B T}\right) \rho^{\alpha}_{M} \left|\dot{\gamma}^{\alpha}\right| \tag{9}$$

where Φ is the family of planes corresponding to a particular slip direction, $\tau^{\star}$ is the critical stress, V_a is the activation volume for cross-slip and k_{cs} is a cross-slip parameter. The first term in Eq. 9 represents the probability of cross-slipping of dislocations from other slip systems in Φ to the slip system α while the second term represents the cross-slipping of dislocations from slip system α to other slip systems in the family of planes. In the present model no distinction between edge and screw dislocation densities has been made, and it is assumed that inelastic deformation occurs due to mobile screw dislocations. A more sophisticated cross-slip model for BCC systems considering edge and screw dislocation densities has been provided in [19].

3 Loop interaction models in the dislocation-density based crystal plasticity framework

Two different models for the interaction of network dislocations with SIA loops have been considered in this work and are described below.

3.1 Distribution of SIA loops on all slip systems: Model-I

In this model [14], the SIA loops are considered on all the BCC slip systems and their effect on the athermal resistance is defined by

$$s_a^\alpha = Gb^\alpha \sqrt{\sum_\beta q_p A^{\alpha\beta} \rho^\beta + q_i N_i^\alpha d_i^\alpha} \tag{10}$$

where q_i is a parameter, N_i^α is the number density of loops on slip system α and d_i^α is the size of the loops. The loops also modify the mean trapping distance of mobile dislocations following

$$\frac{1}{\lambda^\alpha} = \beta_\rho \sqrt{\rho^\alpha} + \beta_i \sqrt{N_i^\alpha d_i^\alpha} \tag{11}$$

where β_i is a scaling parameter. Once the dislocations become glissile by overcoming the loop resistance, they start annihilating the loops. The annihilation of the loops by the mobile dislocations is incorporated via a phenomenological relationship

$$\dot{N}_i^\alpha = -\frac{R_{ann}}{d_i^\alpha b^\alpha} \left(N_i^\alpha d_i^\alpha\right)^c \left(\rho_M^\alpha\right)^{1-c} |\dot{\gamma}^\alpha| \tag{12}$$

where R_{ann} is the annihilation radius and c is a factor.

3.2 Distribution of SIA loops on specific habit planes: Model-II

In this model [15], a second order damage descriptor tensor ($\underline{\underline{H}}$) is utilized to capture the interaction between network dislocations and irradiation induced SIA loops. The damage tensor is defined as

$$\underline{\underline{H}} = \sum_l 3 d_i^l N_i^l \left(\underline{\underline{I}} - \underline{n}_i^l \otimes \underline{n}_i^l\right) \tag{13}$$

where d_i^l is the hexagonal loop diameter, N_i^l is the initial number density of loops and n_i^l are the normals to the loop planes. The annihilation of the loops is defined by

$$\dot{\underline{\underline{H}}} = -\eta \sum_\alpha \left(\underline{\underline{N}}^\alpha : \underline{\underline{H}}\right) \underline{\underline{N}}^\alpha |\dot{\gamma}^\alpha| \tag{14}$$

where η is the scaling factor for annihilation and $\underline{\underline{N}}^\alpha$ is a second order tensor of slip plane normals, $\underline{\underline{N}}^\alpha = \underline{n}_0^\alpha \otimes \underline{n}_0^\alpha$. The form of Eqs.13 and 14 ensures that the loops are not annihilated by mobile dislocations whose slip planes coincide with the habit planes of the loop. The effect of the loops on the athermal resistance is defined as

$$s_a^\alpha = Gb^\alpha \sqrt{\sum_\beta q_p A^{\alpha\beta} \rho^\beta + q_i \underline{\underline{N}}^\alpha : \underline{\underline{H}}} \tag{15}$$

4 Numerical integration of the crystal plasticity model

The dislocation density based crystal plasticity model has been implemented in the Grizzly application under MOOSE [20]. The system of equations provided in Section 2 has been integrated using the implicit backward Euler scheme. Two different integration algorithm has been implemented. In the first algorithm, the residual equation is constructed for the 2^{nd} Piola-Kirchhoff stress in the intermediate configuration [21] and solved using a Newton-Raphson method following

$$\underline{\underline{R}} = \underline{\underline{T}}^* - \underline{\underline{\underline{\underline{E}}}} : \frac{1}{2}\left(\underline{\underline{C}}^e - \underline{\underline{I}}\right) \tag{16a}$$

$$\underline{\underline{\underline{\underline{J}}}} = \underline{\underline{I}} \otimes \underline{\underline{I}} - \frac{1}{2}\underline{\underline{\underline{\underline{E}}}} : \frac{\partial \underline{\underline{C}}^e}{\partial \underline{\underline{T}}^*} \tag{16b}$$

$$\underline{\underline{T_{i+1}}}^* = \underline{\underline{T_i}}^* - \underline{\underline{\underline{\underline{J_{i+1}}}}}^{-1} \underline{\underline{R_{i+1}}} \tag{16c}$$

where $\boldsymbol{R}$ and $\boldsymbol{C}^e$ are the second order residual and right Cauchy-Green tensors respectively, and, $\boldsymbol{J}$ and $\boldsymbol{E}$ are the fourth order Jacobian and elasticity tensors, respectively. The subscripts i and $i+1$ are the Newton-Raphson iterations. In the stress update iterations, the densities of dislocations and loops are kept constant, and are subsequently updated as

$$g_{n+1,i+1} = g_n + \left(g_n, \dot{\gamma}^{\alpha}_{n+1,i+1}\right) \Delta t \tag{17}$$

until the convergence criterion

$$\left| g_{n+1,i+1} - g_{n+1,i} \right| \leq \eta g_n \tag{18}$$

is satisfied. In Eqs. 17 and 18, g represents the state variables and η is a relative tolerance value.

In the second algorithm, the residual equations are constructed for slip rate on individual slip systems [22] and solved using Newton-Raphson iterations as

$$R^{\alpha} = \dot{\gamma}^{\alpha} - h^{\alpha}\left(\tau^{\alpha}, g^{\alpha}\right) \tag{19a}$$

$$J^{\alpha\beta} = \delta^{\alpha\beta} - \frac{\partial h^{\alpha}}{\partial \dot{\gamma}^{\beta}} \tag{19b}$$

$$\dot{\gamma}^{\alpha}_{i+1} = \dot{\gamma}^{\alpha}_{i} - J^{\alpha\beta-1}_{i+1} R^{\alpha}_{i+1} \tag{19c}$$

The densities of dislocations and SIA loops are updated within every Newton-Raphson iteration to solve the slip rate following Eq.17. The second algorithm avoids the additional outer loop to update the state variables that exist in the first algorithm. Hence, this approach allows larger time steps than the first algorithm. However, the factorization operations in this algorithm scale with number of slip systems and can increase the computational cost when compared to the first algorithm, particularly for BCC materials with 48 slip systems.

Additionally, to aid convergence, the evolution of dislocation density via cross-slip is updated following

$$\dot{\rho}^{\alpha}_{CS,n+1,i+1} = \sum_{\beta\in\Phi,\beta\neq\alpha} k_{cs} exp\left(-\frac{\left(\tau^{*} - \left|\tau^{\alpha}_{n}\right|\right) V_a}{K_B T}\right) \rho^{\beta}_{M,n} \left|\dot{\gamma}^{\beta}_{n+1,i+1}\right| - \sum_{\beta\in\Phi,\beta\neq\alpha} k_{cs} exp\left(-\frac{\left(\tau^{*} - \left|\tau^{\beta}_{n}\right|\right) V_a}{K_B T}\right) \rho^{\alpha}_{M,n} \left|\dot{\gamma}^{\alpha}_{n+1,i+1}\right| \tag{20}$$

where τ^{α}_{n} and $\rho^{\alpha}_{M,n}$ are the resolved shear stresses and mobile dislocation densities, respectively, evaluated in the previous increment, n.

Substepping has also been incorporated in the integration algorithms to avoid global time step reduction for local constitutive solve failures. In substepping, the applied deformation gradient is halved recursively following

$$F_{n+1,p} = p\left(F_{n+1} - F_n\right)/2^m + F_n \tag{21}$$

if the local solve fails. In Eq.21, $p \in [1, 2^m]$ and $m \geq 0$ is the substep number.

Further, the flow velocity in Eq.4, having a discontinuity at $|\tau^{\alpha}| - s^{\alpha}_{a} = 0$, has been regularized following

$$v^{\alpha} = l^{\alpha} v \exp\left(-f\left[\left(1 - \left(\frac{|c| + c}{2}\right)^{p}\right)^{q} + \frac{|c| + c}{2\zeta}\right]\right) \tag{22}$$

where $f = \Delta F/\left(K_B T\right)$, $c = \left(|\tau^{\alpha}| - s^{\alpha}_{a}\right)/s^{\alpha}_{t}$ and ζ is a penalty parameter. The regularization addresses convergence issues that can arise because of the discontinuity particularly for small values of f. A comparison of the flow velocity between the unmodified and regularized velocity equation for different ζ values is shown in Fig.3. The comparison has been performed for $l^{\alpha} v = 1$ and $f = 1$. Based on the comparison, $\zeta = 10^{-5}$ has been used in all the simulations.

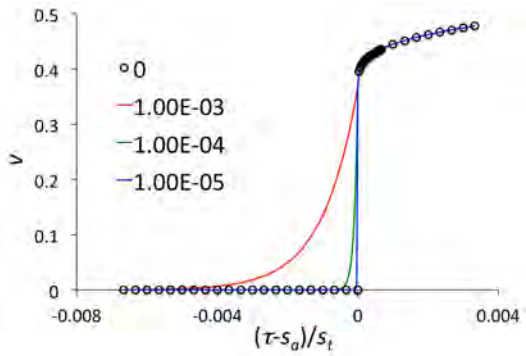

Figure 3: Effect of penalty parameter, ζ, on the regularized flow velocity. $\zeta = 0$ represents the unmodified equation. Values of $l^{\alpha} v = 1$ and $f = 1$ have been considered for comparison.

5 Results and Discussion

5.1 Comparison between the two numerical integration algorithms

A comparison between the two numerical integration algorithms has been performed by loading a single element uniaxially. Symmetric boundary conditions have been applied on the other faces not involved in the uniaxial loading. The parameters provided in [14] have been utilized in this simulation. A value of 10^3 and 0.8 has been used for parameters k_{cs} and c, respectively. The single element has been rotated by 10^o to induce non-symmetricity and cross-slip. A comparison of stress, and, minimum and maximum mobile dislocation densities is shown in Fig.4. The two algorithms provide nearly identical solutions, hence a single curve is shown for the results, and a second curve shows the difference between the solutions.

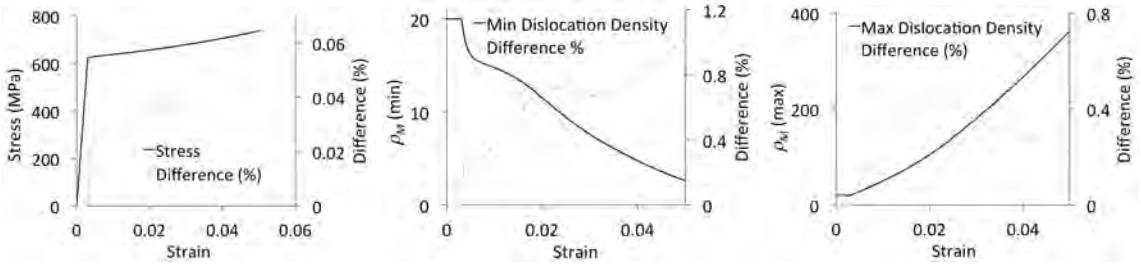

Figure 4: Comparison of (a) stress (b) minimum mobile dislocation density (μm^{-2}), and (c) maximum mobile dislocation density (μm^{-2}), between the two numerical integration algorithms. The percentage difference is calculated as $\left| v_{algorithm1} - v_{algorithm2} \right| / v_{algorithm1}$.

5.2 Effect of cross-slip on the evolution of dislocation densities

The FE model described in Section 5.1 has been utilized to compare the evolution of dislocation densities and stress for various values of the cross-slip parameter, k_{cs}, and is shown in Figs.5, 6 and 7. With higher values of k_{cs}, cross-slip of dislocations to the active slip systems are increased. This can be observed from Fig.5a, where maximum mobile dislocation densities are much higher for larger k_{cs} values and corresponds to slip systems to which dislocations have cross-slipped. Similarly, mobile dislocation densities in the inactive slip systems decrease since they cross-slip to the active slip systems (Fig.5b). For $k_{cs} = 10^4$, cross-slip of almost all the mobile dislocations can be observed from Fig.5b. Immobilization of dislocations is similarly minimized for higher values of k_{cs} since they have a higher propensity to stay mobile via cross-slipping as can be observed from Fig.6a. Additionally, the overall density of immobile dislocations decreases for higher values of k_{cs} due to the added effect of dynamic recovery and is shown in Fig.6b. Since the increase of mobile dislocation densities associated with higher values of k_{cs} is larger (Fig.5a) than the immobilization due to lower k_{cs} values (Fig.6a), the strain-hardening effect is more pronounced for the former case (Fig.7).

5.3 Effect of cross-slip on the annihilation of SIA loops

The single crystal model described in Section 5.1 has been utilized to investigate the influence of cross-slip on annihilation of SIA loops. The presence of loops decreases the mean free path of dislocation trapping following Eq.11, resulting in rapid immobilization of dislocations, as can be observed in Fig.8b. On the activated slip systems where cross-slip can occur, a significant increase in mobile dislocation density can subsequently be observed (Fig.8a), which scales with k_{cs}. Significant trapping of dislocations on the systems

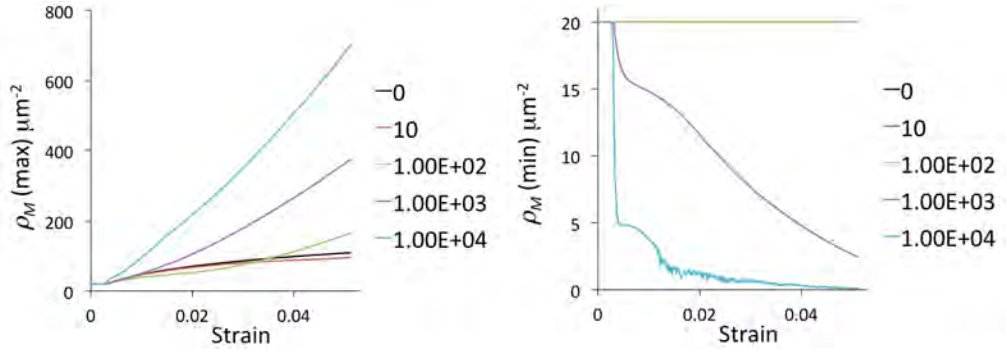

(a) (b)

Figure 5: Effect of cross-slip parameter, k_{cs}, on (a) maximum and (b) minimum mobile dislocation densities.

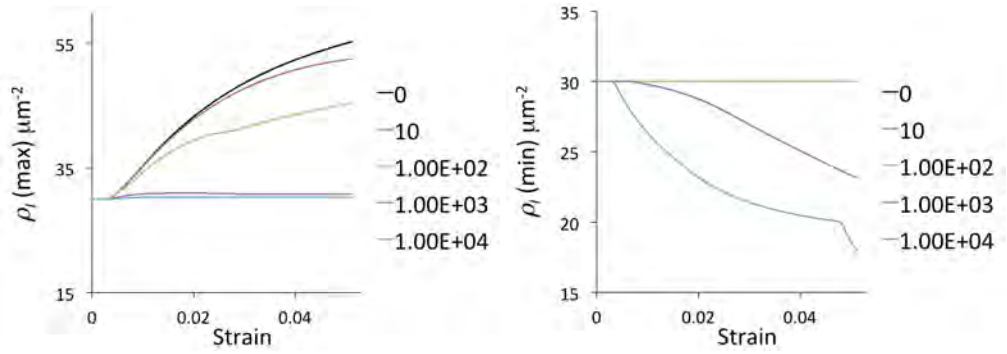

(a) (b)

Figure 6: Effect of cross-slip parameter, k_{cs}, on (a) maximum and (b) minimum immobile dislocation densities.

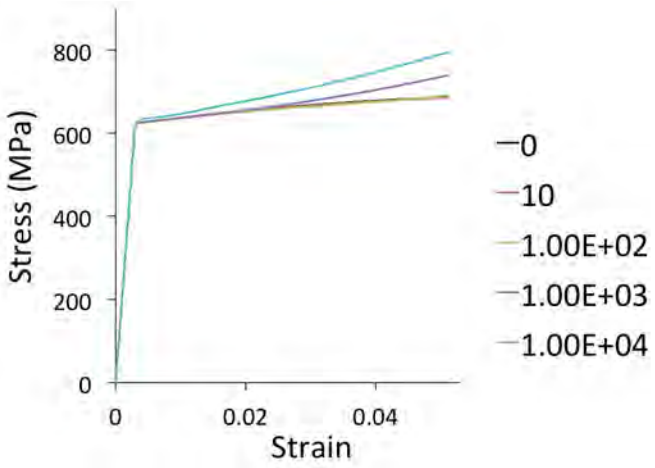

Figure 7: Effect of cross-slip parameter, k_{cs}, on stress.

where cross-slip occurs can also be observed in Fig.9a. The interaction between the cross-slip of mobile dislocations and trapping plays a competitive role as can be observed from the rate of annihilation of SIA loops in Fig.10. Though a higher rate of cross-slipping due to larger k_{cs} values increases the density of mobile dislocations significantly (Fig.8a), increased immobilization decreases the density of mobile dislocations that are required to annihilate the loops. Thus with increasing k_{cs} beyond a critical value (10 in this case), a decrease in the rate of annihilation of SIA loops can be observed in Fig.10. This reduction is also reflected in the evolution of stress (Fig.11). For $k_{cs} = 10^3$ a transition from softening to hardening is also envisaged due to significant increase in the mobile and immobile dislocation densities.

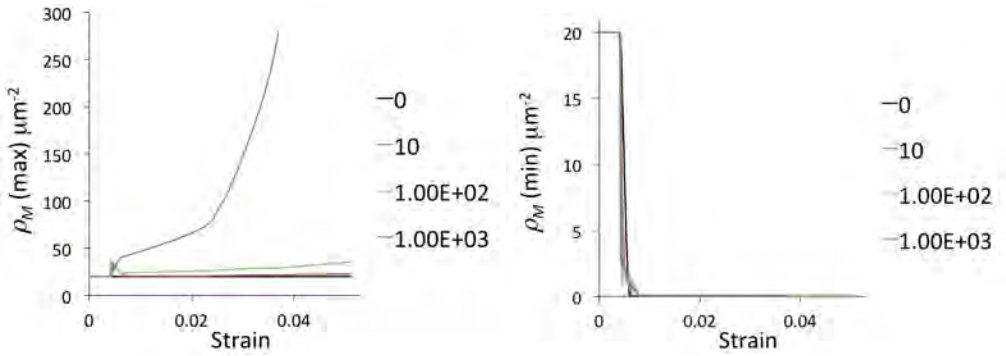

(a) (b)

Figure 8: Influence of cross-slip parameter, k_{cs}, and dislocation trapping on (a) maximum and (b) minimum mobile dislocation densities.

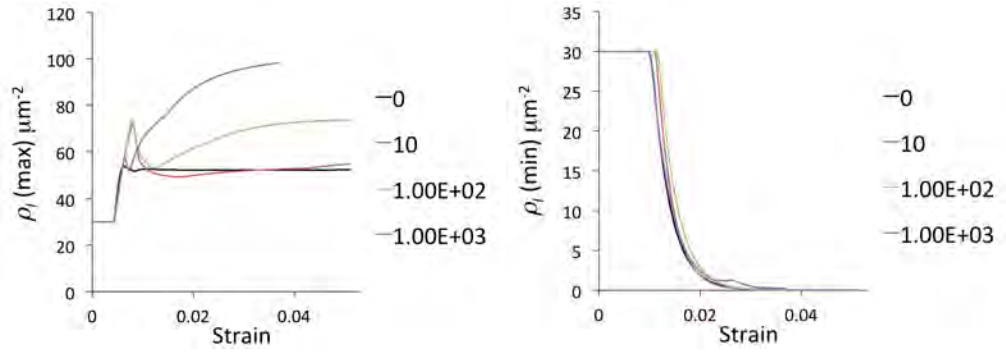

(a) (b)

Figure 9: Influence of cross-slip parameter, k_{cs}, and dislocation trapping on (a) maximum and (b) minimum immobile dislocation densities.

5.4 Validation of Model-I with experiments

The first model is validated with experiments considering a poly-crystalline microstructure with 25 randomly oriented grains and a representative size of $25\mu m \times 25\mu m \times 25\mu m$. The poly-crystalline microstructure is discretized using a mesh size of $1\mu m$ and is shown in Fig.12. The microstructure is uniaxially strained along the y-direction and minimally restrained along the other directions. The values of the parameters provided in [14] have been used for validation, except for k_{cs} for which a value of 100 has been considered. Also, 3D FE simulations have been performed here in contrast to 2D generalized plane strain FE simulations in [14].

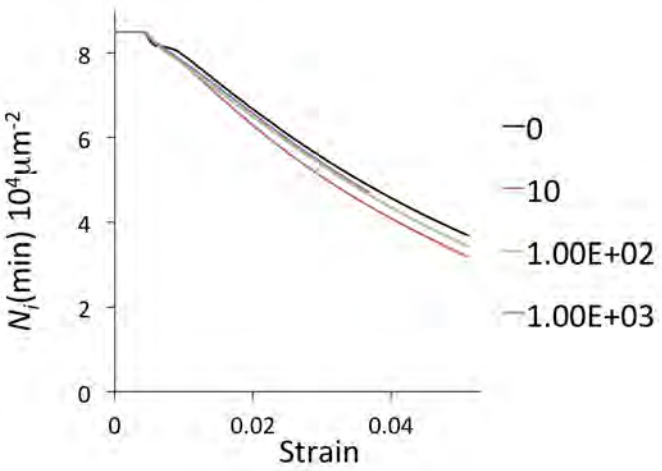

Figure 10: Influence of cross-slip parameter, k_{cs}, and dislocation trapping on SIA loop annihilation. The evolution of the minimum loop density is presented in the figure.

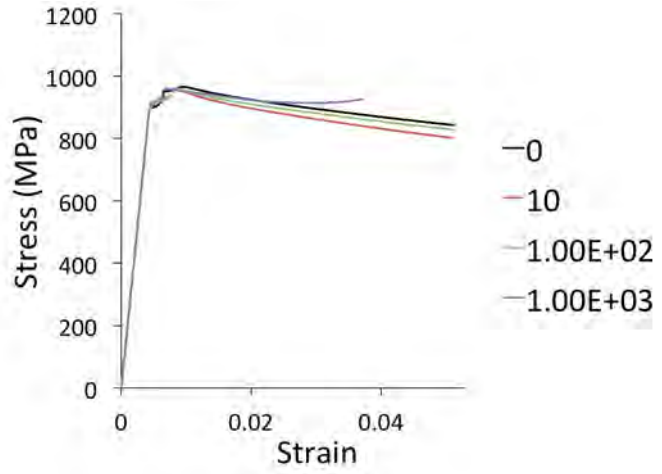

Figure 11: Influence of cross-slip parameter, k_{cs}, and dislocation trapping on stress.

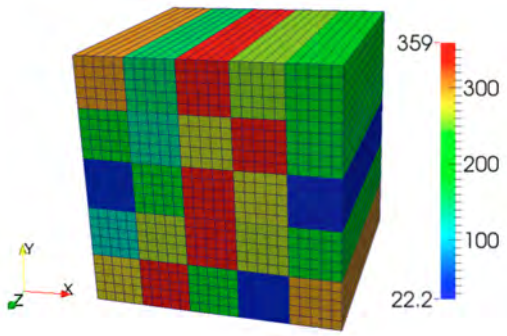

Figure 12: Distribution of Euler angle (ψ in degrees following Bunge) in the representative poly-crystalline microstructure and the FE mesh. The size of the representative volume is $25\mu m \times 25\mu m \times 25\mu m$.

A comparison of the engineering stress-strain response for the unirradiated Mod 9Cr-1Mo F/M steel [16] at two different temperatures is shown in Fig.13. As can be observed from the figure, the dislocation density-based crystal plasticity model is able to capture the stress-strain evolution satisfactorily. The distribution of stress, equivalent plastic strain and maximum mobile dislocation density for T = 437 K at 5% strain is shown in Fig.14. As can be observed from the figure, the microstructure undergoes a heterogeneous evolution of state that strongly depends on the orientation of crystals in the poly-crystalline microstructure. Such heterogeneous evolution strongly influences the localization of damage, which will be considered in future studies.

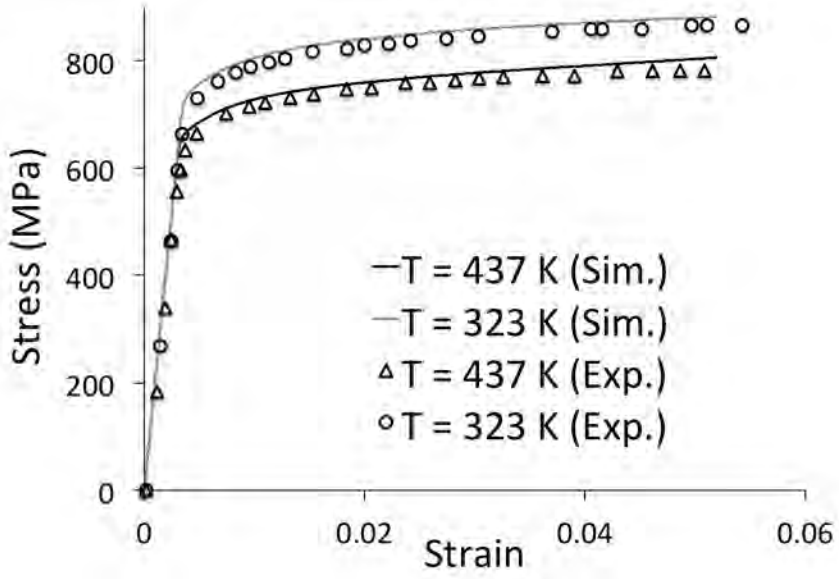

Figure 13: Comparison of engineering stress strain between dislocation density based crystal plasticity model and experiments for unirradiated Mod 9Cr-1Mo F/M steel.

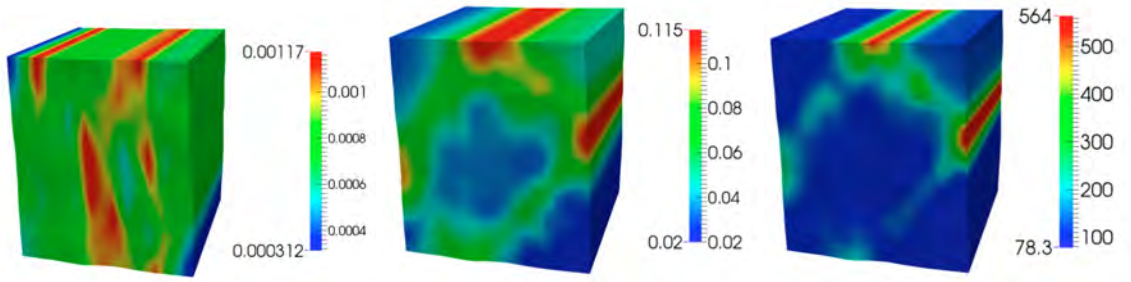

(a) (b) (c)

Figure 14: Distribution of (a) stress$\times 10^6$ (MPa), (b) equivalent plastic strain and (c) maximum mobile dislocation density $\left(\mu m^{-2}\right)$, for T = 437 K at 5% strain.

The effect of irradiation on the stress-strain behavior has been validated for the same material irradiated to different dose-levels (2.9 and 0.9 dpa) and tested at two different temperatures (437 and 323 K) [16]. In the FE simulations, a much smaller mesh size (0.33 μm) has also been utilized, consistent with the width of the clear channels observed experimentally. The values $q_i = 0.2$ and $k_{cs} = 1$ has been used in these simulations different from [14]. For T = 437 K and dpa = 2.9, a SIA loop density of $8.5\times 10^{13} m^{-3}$ and size 6.3 nm has

been used from [23]. For T = 323 K and dpa = 0.9, a smaller loop density of $8.1\times10^{13}m^{-3}$ and size 6.0 nm has been utilized.

The comparison of the engineering stress-strain is shown in Fig.15a. As can be observed from the figure, very little uniform strain is present for both the conditions and is satisfactorily captured by the model. A comparison of the engineering stress-strain evolution for various mesh sizes is shown in Fig.15b. The stress-strain evolution prior to softening is almost identical for both mesh sizes. However, a higher softening rate can be observed for the finer mesh, in which localization is more severe and is typical for local models developed presently.

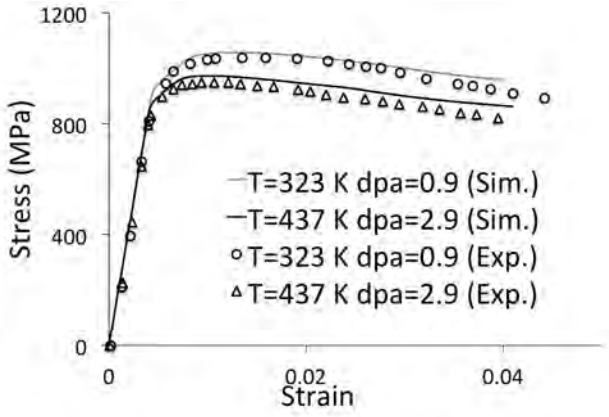

(a)

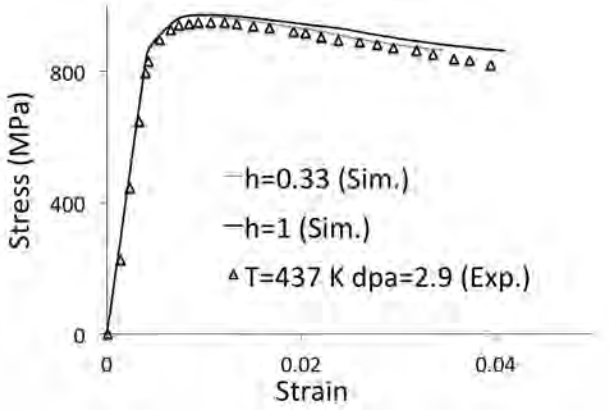

(b)

Figure 15: Comparison of engineering stress-strain between (a) dislocation density based crystal plasticity model and experiments, (b) two different mesh size (h in μm), for radiated Mod 9Cr-1Mo F/M steel.

The distribution of plastic strain and minimum SIA loop density at ≈3.5% strain is shown in Fig.16. From this figure, the formation of localization bands due to the annihilation of SIA loops by the mobile dislocations is evident. Also, the formation of clear channels can be observed to be strongly dependent on crystal orientations (Fig.16). Capturing such anisotropy is only possible through the use of crystal plasticity-based models and justifies its use in this work.

5.5 Comparison of Model-II with dislocation dynamics simulations

The comparison of the second model (Section 3.2) with DD simulations is presented in [17]. In the current implementation of this model, inelastic deformation is described using dislocation densities instead of phe-

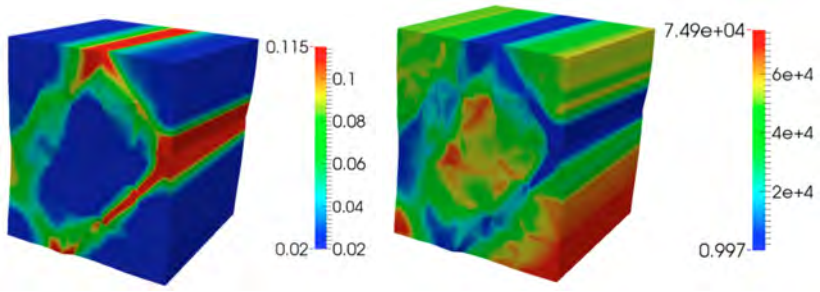

Figure 16: Distribution of (a) equivalent plastic strain and (b) minimum SIA loop number density $\left(\mu m^{-3}\right)$, for radiated sample at 2.9 dpa and T = 437 K. The contour plot is at ≈3.5% strain level.

nomenological evolution of slip resistances and is a diversion from the original formulation [15]. Prior to this comparison, the parameter q_i (Eq.15) has been calibrated from DD simulations for the $N_i^l = 0$ case, and, the initial mobile and immobile dislocation densities are assigned values of $10^7 mm^{-2}$. The values of all other parameters have been obtained from [14]. Cross-slip has also been neglected in the verification, consistent with the DD simulations. The single crystal FE model described in Section 5.1 has been utilized for the model verification. A comparison of the stress-equivalent plastic strain between the crystal plasticity and DD simulations is shown in Fig. 17. As can be observed from the figure, the crystal plasticity model is able to capture the increase in yield stress and the post-yield hardening/softening behavior satisfactorily, with minimum calibration of parameters.

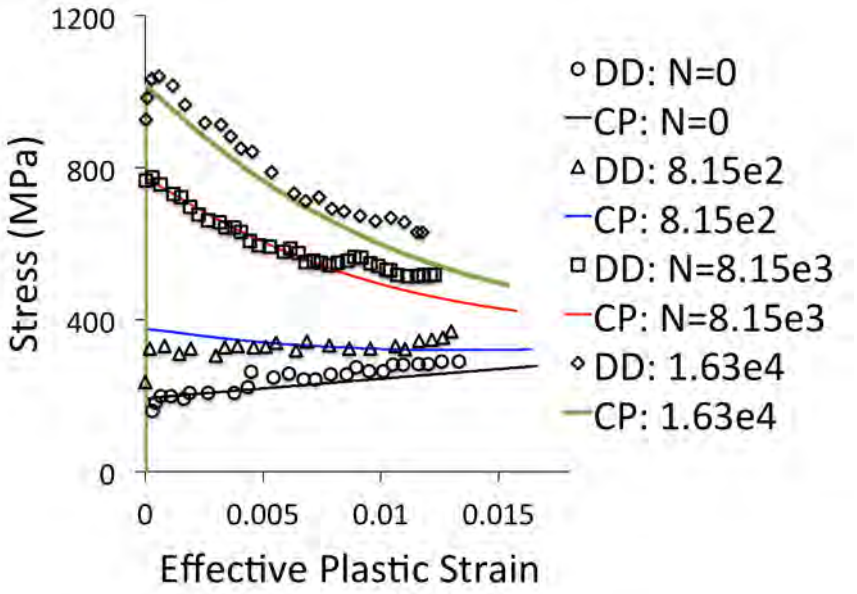

Figure 17: Comparison of stress-equivalent plastic strain between dislocation density based crystal plasticity (CP) model and DD simulations. In the figure, N represents the number density of SIA loops in μm^{-3}.

6 Summary

In this report, a dislocation-density based crystal plasticity model has been developed in Grizzly. This model captures the effect of irradiation-induced defects on the flow stress behavior of ferritic and ferritic/martensitic steels. The formulation incorporates the interaction between self-interstitial loops and matrix dislocations. Such interactions lead to an increase in the yield stress and softening at higher strain levels due to defect annihilation. Two different algorithms have been implemented to numerically integrate the evolution equations in the crystal plasticity formulation and have been compared. The present formulation also incorporates cross-slip, which is pertinent in BCC systems. Finite element simulations of representative microstructures have been performed and the predictions from the model have been compared with experiments at different test temperatures and irradiation dose levels.

Future work will focus on effect of precipitation on the flow stress in RPV steels. After incorporating the relevant hardening/softening mechanisms, extensive comparison with experimental data of flow stress for RPV steels will be made. The framework will also allow modeling of cleavage micro-crack initiation and propagation at the length scale of poly-crystals, and will be considered in future efforts under Grizzly.

7 References

1. C. English and J. Hyde. *Radiation Damage of Reactor Pressure Vessel Steels*, volume 4, chapter 4.05, pages 151–180. Elsevier, 2012.

2. E. Eason, G. R. Odette, R. Nanstad, and T. Yamamoto. A physically based correlation of irradiation-induced transition temperature shifts for rpv steels. Oak Ridge Report ORNL Report ORNL/TM-2006/530, Oak Ridge National Lab., 2007.

3. Editorial. Perfect - prediction of irradiation damage effects on reactor components: A summary. *Journal of Nuclear Materials*, 406:2–6, 2010.

4. A. L. Gurson. Continuum theory of ductile rupture by void nucleation and growth: Part I-yield criteria and flow rules for porous ductile media. *Journal of Engineering Materials*, 99:2–15, 1997.

5. G. Rousselier. Ductile fracture models and their potential in local approach of fracture. *Nuclear Engineering and Design*, 105:97–111, 1987.

6. F.M. Beremin. A local criterion for cleavage fracture of a nuclear pressure vessel steel. *Metals and Materials Transaction A*, 14A:2277–2287, 1983.

7. W. Weibull. A statistical distribution function of wide applicability. *Journal of Applied Mechanics*, 18:293–297, 1953.

8. B. Tanguy, J. Besson, R. Piques, and A. Pineau. Ductile to brittle transition of an A508 steel characterized by Charpy impact test. Part II: modeling of the Charpy transition curve. *Engineering Fracture Mechanics*, 72:413–434, 2005.

9. B. Tanguy, C. Bouchet, S. Buget, and J. Besson. Local approach to fracture based prediction of the ΔT_{56J} and $\Delta T_{KIC,100}$ shifts due to irradiation for an a508 pressure vessel steel. *Engineering Fracture Mechanics*, 73(191-206), 2006.

10. M. K. Samal, M. Seidenfuss, E. Roos, B. K. Dutta, and H. S. Kushwaha. Experimental and numerical investigation of ductile-to-brittle transition in a pressure vessel steel. *Material Science and Engineering A*, 496:25–35, 2008.

11. P. Chakraborty and S. B. Biner. Parametric study of irradiation effects on the ductile damage and flow stress behavior in ferritic-martensitic steels. *Journal of Nuclear Materials*, 465:89–96, 2015.

12. G. R. Odette, M. Y. He, and T. Yamamoto. On the relation between irradiation induced changes in the master curve reference temperature shift and changes in strain hardened flow stress. *Journal of Nuclear Materials*, 367-370:561–567, 2007.

13. S. J. Zinkle and B. N. Singh. Microstructure of neutron-irradiated iron before and after tensile deformation. *Journal of Nuclear Materials*, 351:269–284, 2006.

14. A. Patra and D. L. McDowell. Continuum modeling of localized deformation in irradiated bcc materials. *Journal of Nuclear Materials*, 432:414–427, 2013.

15. N. R. Barton, A. Arsenlis, and J. Marian. A polycrystal plasticity model of strain localization in irradiated iron. *Journal of the Mechanics and Physics of Solids*, 61:341–351, 2013.

16. S. A. Maloy, M. R. James, G. Willcutt, W. F. Sommer, M. Sokolov, L. L. Snead, M. L. Hamilton, and F. Garner. The mechanical properties of 316l/304l stainless steels, alloy 718 and mod 9cr±1mo after irradiation in a spallation environment. *Journal of Nuclear Materials*, 296:119–128, 2001.

17. A. Arsenlis, M. Rhee, G. Hommes, R. Cook, and J. Martin. A dislocation dynamics study of the transition from homogeneous to heterogeneous deformation in irradiated body-centered cubic iron. *Acta Materialia*, 60:3748–3757, 2012.

18. F. Roters, P. Eisenlohr, L. Hantcherli, D. D. Tjahjanto, T. R. Bieler, and D. Raabe. Overview of constitutive laws, kinematics, homogenization and multiscale methods in crystal plasticity finite-element modeling: Theory, experiments, applications. *Acta Materialia*, 58:1152–1211, 2010.

19. A. Alankar, D. P. Field, and D. Raabe. Plastic anisotropy of electro-deposited pure α-iron with sharp crystallographic $\langle 111 \rangle //$ texture in normal direction: Analysis by an explicitly dislocation-based crystal plasticity model. *International Journal of Plasticity*, 52:18–32, 2014.

20. INL. Multi-physics object oriented simulation environment (MOOSE), 2008.

21. S. Balasubramanian. *Polycrystalline Plasticity: Application to Deformation Processing of Lightweight Metals*. PhD thesis, Massachusetts Institute of Technology, 1998.

22. X. Ling, M. F. Horstemeyer, and G. P. Potirniche. On the numerical implementation of 3d rate-dependent single crystal plasticity formulations. *International Journal form Numerical Methods in Engineering*, 65:548–568, 2005.

23. C. Deo, C. Tome, R. Lebensohn, and S. Maloy. Modeling and simulation of irradiation hardening in structural ferritic steels for advanced nuclear reactors. *Journal of Nuclear Materials*, 377:136–140, 2008.